Quantitative Analysis of Structure-related Spatial Harmonics on Torque Generation in Hybrid Excited Asymmetric Stator Pole Double Salient Machine for Integrated Machine Drive Applications

Chen Cao, Wei Xu, *Fellow*, *IEEE*, Jian Ge, *Member*, *IEEE*, Bin Du, Zhongyong Chen, Chuanjia Zhang, Lili Kang, and Lei Zhang

***Abstract*—With the rapid development of integrated machine drives (IMDs), hybrid excited asymmetric stator pole double salient machines (HEASPDSMs) have gained widespread attention owing to their flexible flux regulation ability, excellent heat dissipation capacity, and robust structure. As a type of flux modulation machine, HEASPDSMs exhibit numerous magnetic field harmonics due to their double-sided reluctance structure and introduction of asymmetric stator poles and excitation windings. These harmonics cause significant distortions in airgap flux density, back-electromotive-force (back-EMF), and torque. Traditional magnetomotive force (MMF)-specific permeance analytical methods fail to quantify the torque contribution of individual structural-related spatial harmonics, which restricts the torque density improvement of HEASPDSMs. To mitigate the torque distortion and improve torque density, a novel evaluation model for both average torque and torque ripple of HEASPDSMs is proposed in this paper. Different from classical methods, the proposed model directly utilizes stator/rotor MMF and specific permeance as modulation components for torque calculation, which can quantitatively clarify the individual contribution of each modulation harmonic to torque and establish a direct correlation between harmonic contribution and structural parameters. Furthermore, its accuracy is validated via finite element analysis (FEA) by performing single-parameter-scan on four HEASPDSMs with different pole-pair combinations, during which the torque performance and flux regulation ability are analyzed. Finally, experimental validation is performed on a 12s7p HEASPDSM prototype to further verify the proposed model.**

***Index Terms*—Hybrid excited asymmetric stator pole double salient machine (HEASPDSM), integrated machine drive (IMD), structure-related spatial harmonics, torque model.**

Manuscript received January 18, 2026; revised March 18, 2026; accepted March 25, 2026. Date of publication June 25, 2026.Date of current version April 13, 2026.

This work was supported in part by the National Natural Science Foundation of China under Grants 52277050 and 52407050, the High-level Talent Program at Chinese Academy of Sciences under Grant E42K0801, the Fundamental and Interdisciplinary Disciplines Breakthrough Plan of the Ministry of Education of China under Grant JYB2025XDXM203, the Foundation of State Key Laboratory of High-Density Electrical Energy Conversion under Grant DN202509, and the Foundation of State Key Laboratory of High Density Electromagnetic Power and Systems under Grant 2025KFZD003 .

Chen Cao is with the State Key Laboratory of Advanced Electromagnetic Technology, Huazhong University of Science and Technology, Wuhan 430000, China (e-mail: chencao@hust.edu.cn).

Wei Xu is with the State Key Laboratory of High Density Electromagnetic Power and Systems, Institute of Electrical Engineering, Chinese Academy of Sciences, Beijing 100190, China (e-mail: weixu@mail.iee.ac.cn).

Jian Ge is with the State Key Laboratory of High-Density Electrical Energy Conversion, Huazhong University of Science and Technology, Wuhan 430074, China (e-mail: gejian1994@hust.edu.cn).

Bin Du is with the China National Electric Apparatus Research Institute Co., Ltd., Guangzhou 510000, China (e-mail: dub@cei1958.com).

Zhongyong Chen is with the School of Electrical and Electronic Engineering, Huazhong University of Science and Technology, Wuhan 430000, China (e-mail: zychen@hust.edu.cn).

Chuanjia Zhang is with the Electromechanical Apparatus and Equipment Division of CVC Testing Technology Co., Ltd., Guangzhou 510000, China (e-mail: zhangchj@cvc.org.cn).

Lili Kang is with the Intelligent Manufacturing College, Tianjin Sino-German University of Applied Sciences, Tianjin 300350, China (e-mail: kanglili0501@163.com).

Lei Zhang is with the CRRC Tangshan Co., Ltd., Tangshan 063000, China. (e-mail: crh350@163.com).

(*Corresponding Author*: *Wei Xu*)

Digital Object Identifier 10.30941/CESTEMS.2026.00014

NOMENCLATURE

B_g	Airgap flux density
D_{ri}	Inner diameter of rotor
D_{so}	Outer diameter of stator
E_{ABC}	Three-phase voltage
F	Magnetomotive force (MMF)
F_k	Fourier coefficient of MMF
F_{pm}	MMF amplitude of permanent magnets (PMs)
g	Airgap length
H_{bridge}	Height of magnetic bridge
H_{pm}, H_{sy}, H_{ry}	Heights of PMs, stator yoke and rotor yoke
i_d, i_q	Currents in d- and q- axis
I_c, I_e	Armature and excitation currents
I_m	Amplitude of armature current
I_{ABC}	Three-phase current
K_{lpm}, K_{le}	Leakage coefficients of PMs and excitation winding
K_ψ	Flux regulation coefficient
k_{slot}	Slot fill factor (copper)
L	Stack length
M_{ce}	Mutual inductance for two windings
n	Rated speed
N_A	Winding function of phase A

N_c, N_e	Turns of armature winding and excitation winding
N_h	Fourier coefficient of winding function
N_s, N_r	Number of stator teeth and rotor poles
R_g, R_{pm}, R_e	Magnetic reluctance in airgap, PMs and excitation winding
R_{si}	Inner radius of stator
R_{ro}	Outer radius of rotor
T_{avg}, T_{rip}	Average torque and torque ripple
T_{max}, T_{min}	Maximum and minimum torques
W_{pm}, W_{rp}, W_{sp}	Widths of PMs, stator tooth, and rotor pole
α, α^*	Slot pitch angles of the excitation winding (asymmetry angle) and the armature winding
β_s, b_{ro}	Radians of stator tooth and rotor poles
γ	Circumferential radian of single PM
$\lvert\Lambda\rvert$	Unit specific permanence
$\Lambda_s, \Lambda_r, \Lambda_g$	Specific permanence of stator, rotor, and airgap
$\Lambda_{s0}, \Lambda_{si}, \Lambda_{r0}, \Lambda_{rj}$	Fourier coefficients of specific permanence for stator side and rotor side
μ_0	Permeability of vacuum
θ_0	Initial angle of rotor
θ_s	Angular degree
ω_r, ω_e	Mechanical and electrical speeds
ψ_A	Flux linkage of phase A
ψ_{pm}	PM flux linkage
$\psi_{enhanced}, \psi_{weakened}$	Enhanced flux linkage and weakened flux linkage

I. INTRODUCTION

THE integrated machine drives (IMDs) are transformative for modern electric drive systems, integrating electric machines, power converters, and control units into a single assembly [1]-[3]. This integration removes external control equipment and long machine-converter connections, offering key advantages in efficiency and compactness. Meanwhile, the double salient permanent magnet motor (DSPM) is characterized by short end windings, strong mechanical robustness, and excellent heat dissipation capacity, and thus has extremely high application value in various IMD occasions such as electrical vehicles (EVs) and electric aircraft [4]-[6]. However, traditional DSPMs rely on permanent magnets (PMs) for excitation exhibit constrained flux regulation and speed expansion capabilities, which are critical requirements for EVs that demand flexible flux control and wide operational speed ranges. A large number of scholars have conducted in-depth research on this issue and introduced the concept of hybrid excitation into this type of motor [7]-[10]. In [7], a 12s8p square hybrid excited double salient machine (HEDSM) is presented. In addition to the armature winding, a set of excitation winding is also present on the stator. By adjusting the magnitude and direction of the excitation current, the amplification or suppression of the PM flux linkage can be accomplished. At the same time, to improve the flux regulation ability, an iron core magnetic bridge arranged in parallel with the PM is added. To further augment the flux regulation capability, as presented in [8], a parallel branch is incorporated into two sets of excitation magnetic circuits for a 6s4p HEDSM, while the branch is realized by adding an additional air gap in the direct current (dc) excitation magnetic circuit. A parallel magnetic circuit type HEDSM is put forward in [9], while the PM magnetic circuit and the dc excitation magnetic circuit are completely decoupled. In [10], a high torque density HEDSM with PMs at the bottom of the sub-slots is proposed, which can relieve the saturation of the yoke and the additional slot-PM flux can establish a parallel excitation path. However, the aforementioned HEDSMs all exhibit unipolar flux linkage, which limits the improvement of the motor's power density. To solve this problem, in [11], a hybrid excited asymmetric stator pole double salient machine (HEASPDSM) with bipolar flux linkage by adjusting the distribution of armature coils is proposed, and an asymmetric stator pole structure is introduced, which allows for flexible adjustment of the slot area occupied by the two sets of windings and effectively enhances the torque and flux regulation performance.

For HEDSM and other motors with multiple working harmonics (magnetic field harmonics which contribute to the average torque), the magnetic field modulation analysis approach (MFMA) is the most commonly utilized analysis method. In [12], the theory of MFMA was systematically presented, and the modulation process of the magnetomotive force by the stator and rotor teeth was expounded in detail. In [9], the no-load airgap magnetic field of a 12s7p HEDSM was subjected to analytical investigation by employing MFMA, and the generation process of each harmonic was elaborated in detail. In [13]-[14], the back-electromotive-force (back-EMF) and torque generation mechanism of magnetic field modulated motors were analyzed, and in [15], the impacts of harmonics of flux density on the output performance are explained. Based on the quantitative analysis of the working harmonics, [16] obtained the general expression of average torque for the consequent-pole permanent magnet machines (CPM). In [17], the torque ripple of a vernier permanent magnet motor (VPM) was analyzed. And in [18]-[19], the stator teeth were optimized based on the positive effect of the specific harmonics of the stator specific permeance on the torque of the VPM.

However, in terms of the application of MFMA in HEDSM, the studies on the torque mostly remain at identifying the working harmonics of the airgap flux density, while it is difficult to correlate the research on flux density components with structural design. In particular, for HEASPDSM, the special structure of the asymmetric stator poles and excitation winding makes this phenomenon more obvious. Meanwhile, the quantitative analysis of the functions that each harmonic of each modulation component exerts in the process of torque generation is necessary, and the current research in this regard is incomplete.

In response to the above problems, this paper proposes a novel torque evaluation model for HEASPDSMs that can quantitatively reflect the influence of structure-related spatial harmonic distribution variation on torque performance. The core feature of the model is that it directly takes stator/rotor magnetomotive force (MMF) and specific permeance as modulation components to screen effective working harmonics, which not only realizes the quantitative evaluation

of the individual contribution of each modulation harmonic to torque generation, but also establishes a direct correlation between harmonic contribution and motor structural parameters. The subsequent structure of the article is as follows. In Section II, a certain type of HEASPDSM with different slot-pole combinations is selected, and its topological characteristics and operating principles are introduced. In Section III, by employing the MFMA, the novel torque model is obtained and the working harmonics of different modulation components are quantitative analyzed. In Section IV, the accuracy of the torque model is validated via FEA through single-parameter scans on four HEASPDSMs with different pole-pair combinations, involving the analysis of how various parameters affect performances such as average torque, torque ripple, and flux regulation ability as part of the validation process. In Section V, the torque model is experimentally verified based on a 12s7p HEASPDSM prototype. Finally, a summary of the article is presented.

II. Topology Analysis of HEASPDSM

As depicted in Fig. 1, the four common slot-pole combinations of HEASPDSM are presented, where the rotors have 5, 7, 8, and 10 poles respectively, and the stator consists of six π-shaped iron cores and six tangentially magnetized PMs arranged alternately along the circumference. Moreover, on the outer side of each permanent magnet (the part encircled in Fig. 1), there is a parallel iron core magnetic bridge. This configuration can effectively enhance the flux regulation capability of the motor.

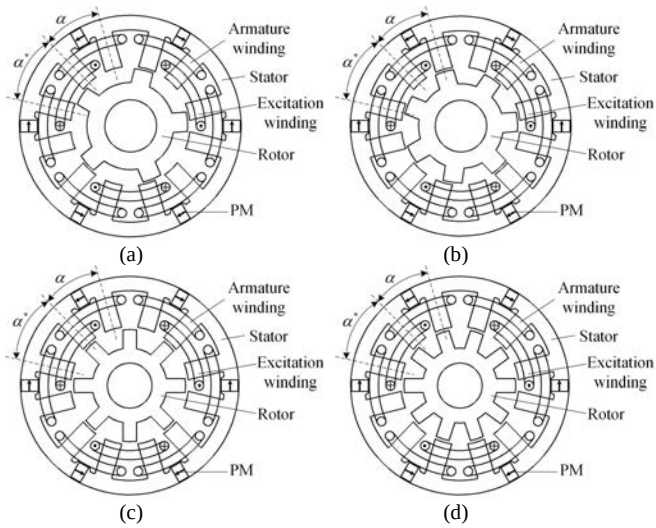

Fig. 1. The HEASPDSM with different slot-pole combinations. (a) 12s5p. (b) 12s7p. (c) 12s8p. (d) 12s10p.

The HEASPDSM can be simplified as Fig. 2, in which the red dash line represents the flux rooted by PMs and the blue dash line is dc excitation winding. The stator is equipped with two sets of windings, namely a double-layer armature winding and a single-layer excitation winding. The magnetic circuit of the excitation winding is connected in series with that of the PMs. When the magnetic flux linkage of the excitation winding is in the same direction as the permanent magnet flux linkage, the motor operates under the flux enhancing condition as shown in Fig. 2(a). Conversely, when the excitation flux linkage is opposite to the PM flux linkage, the motor operates in the flux-weakening condition as shown in Fig. 2(a). Thus, compared with the DSPM and the PMSM, the HEASPDSM has more flexible flux regulation ability, significantly reducing the control difficulty of the motor. Regarding the armature winding, each phase winding consists of two coils. Each coil is wound on two adjacent stator teeth. During the rotation of the rotor, when the rotor pole is aligned with different stator teeth, the armature coils are linked with excitation flux linkages in different directions. That is, the flux linkage of the armature winding is bipolar, which is effectively enhancing the torque density of the motor.

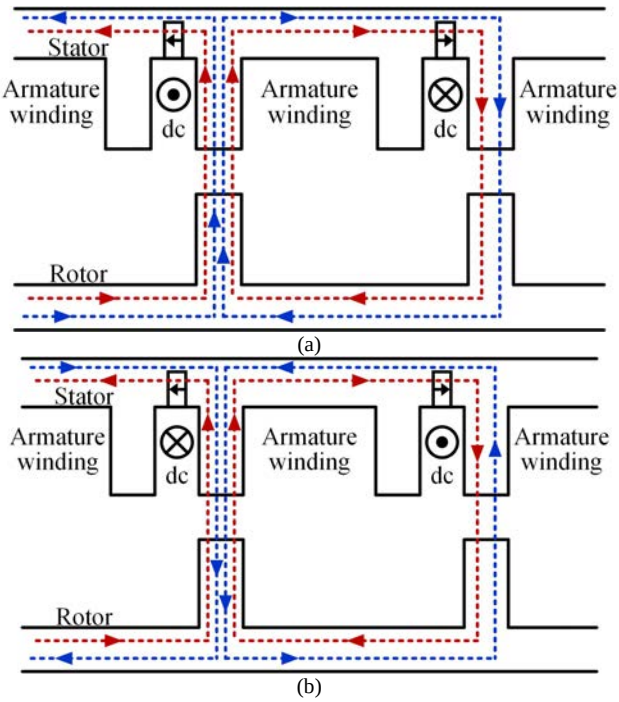

Fig. 2. Flux regulation principle. (a) Flux enhancing. (b) Flux weakening.

Furthermore, the slot pitch angles of the excitation and the armature windings are denoted as α and α^* respectively, with $\alpha+\alpha^*=60°$. Under the premise of keeping the slot fill factor of the motor unchanged, by employing an asymmetric stator slot structure, the performance of the motor can be further enhanced. And the main parameters of the aforementioned topologies utilized in the subsequent analysis are presented in Table I.

III. Analytical Model of HEASPDSM

Prior to analyzing the electromagnetic torque of the motor based on the magnetic field modulation theory, the motor model requires appropriate simplifications as follows:

1) Neglect the saturation effect and disregard the magnetic voltage drop across the iron core.

2) Disregard the end effect of the windings.

3) Assume that the stator and rotor slots are infinitely deep.

4) Ignore the eddy current loss of the PMs.

5) Taking the center line of the permanent magnet as the coordinate origin and the zero point.

TABLE I
MAIN PARAMETERS OF HEASPDSMS

Parameter	Symbol	Value			
		12s5p	12s7p	12s8p	12s10p
Rated speed/(r/min)	n	600			
Outer diameter of stator/mm	D_{so}	120			
Stack length/mm	L	100			
Airgap length/mm	g	0.5			
Height of stator yoke/mm	H_{sy}	8			
Height of magnetic bridge/mm	H_{bridge}	0.5			
Height of PM/mm	H_{pm}	9.4			
Width of PM/mm	W_{pm}	6.1			
Inner diameter of rotor/mm	D_{ri}	28			
Height of rotor yoke/mm	H_{ry}	9.2			
Slot fill factor (copper)	k_{slot}	0.6			
Asymmetry angle/°	α	30	28	26	22
Width of stator tooth/mm	W_{sp}	10	9.5	10.5	9
Outer radius of rotor/mm	R_{ro}	32	33	32	32
Width of rotor pole/mm	W_{rp}	14	10	10	6
Armature current (root-mean-square (RMS))/A	I_c	3			
Excitation current/A	I_e	4			

A. No-load Airgap Flux Density

The MMF waveforms produced by the two sets of excitation sources can be expressed as:

$$\begin{cases} F(\theta_s)=\sum_{k=1}^{3,5,7,\cdots} F_k \sin\left(\frac{kN_s}{4}\theta_s\right) \\ F_k=\frac{R_g}{2R_g+K_{lpm}R_{pm}}\frac{4F_{pm}}{k\pi}\cos\left(\frac{kN_s}{8}\gamma\right) \\ +\frac{R_g}{2R_g+K_{le}R_e}\frac{16N_eI_e}{(\alpha-\beta_s)\pi k^2N_s}\sin\left(\frac{kN_s}{8}(\alpha-\beta_s)\right) \end{cases} \tag{1}$$

where F is the MMF; I_e is the excitation current; γ is the circumferential radian of PMs, β_s is the radian of stator tooth; F_k, θ_s, and N_s are the Fourier coefficient, the angular degree and the number of stator teeth, respectively; k is the Fourier order; F_{pm} is the MMF amplitude of PMs; N_e is the turns of excitation winding; R_g, R_{pm}, and R_e are the magnetic reluctances in airgap, PMs, and excitation winding, respectively; K_{1pm} and K_{1e} are the leakage coefficients of PMs and excitation winding, respectively.

Next, the specific permanence could be deduced to:

$$\begin{cases} \Lambda_s(\theta_s)=\frac{\Lambda_{s0}}{2}+\sum_{i=1}^{\infty}\Lambda_{si}\cos\left(\frac{iN_s}{2}\theta_s\right) \\ \Lambda_{si}=\frac{N_s}{\pi}\left[\int_0^{\frac{\alpha-\beta_s}{2}}\frac{\mu_0}{g+\frac{\pi}{2}R_{si}(\frac{\alpha-\beta_s}{2}-\theta_s)}\cos(\frac{iN_s}{2}\theta_s)\mathrm{d}\theta_s+\right. \\ \int_{\frac{\alpha-\beta_s}{2}}^{\frac{\alpha+\beta_s}{2}}\frac{\mu_0}{g}\cos(\frac{iN_s}{2}\theta_s)\mathrm{d}\theta_s+ \\ \left.\int_{\frac{\alpha+\beta_s}{2}}^{\frac{2\pi}{N_s}}\frac{\mu_0}{g+\frac{\pi}{2}R_{si}\left(\theta_s-\frac{\alpha+\beta_s}{2}\right)}\cos\left(\frac{iN_s}{2}\theta_s\right)\mathrm{d}\theta_s\right] \end{cases} \tag{2}$$

$i=0,1,2,3,\cdots$

$$\begin{cases} \Lambda_r(\theta_s,t)=\frac{\Lambda_{r0}}{2}+\sum_{j=1}^{\infty}\Lambda_{rj}\cos\left(jN_r(\theta_s-\theta_0-\omega_r t)\right) \\ \Lambda_{rj}=\frac{2N_r}{\pi}\left[\int_0^{\frac{b_{ro}}{2}}\frac{\mu_0}{g+\frac{\pi}{2}R_{ro}\left(\frac{b_{ro}}{2}-\theta_s\right)}\cos\left(jN_r\theta_s\right)\mathrm{d}\theta_s+\right. \\ \left.\int_{\frac{b_{ro}}{2}}^{\frac{\pi}{N_r}}\frac{\mu_0}{g}\cos\left(jN_r\theta_s\right)\mathrm{d}\theta_s\right] \end{cases} \tag{3}$$

$j=0,1,2,3,\cdots$

where Λ_s, Λ_r, and Λ_g are specific permanence of stator, rotor, and airgap, respectively; $\Lambda_{s0}, \Lambda_{si}, \Lambda_{r0}$, and Λ_{rj} are the Fourier coefficients; i and j are the Fourier orders; μ_0 is the permeability of vacuum; g is the airgap length; θ_0 is the initial angle; N_r and b_{ro} are the number of rotor poles and the radian of rotor slot, respectively; R_{si} and R_{ro} the inner radius of stator and the outer radius of rotor, respectively; ω_r is the mechanical speed. Furthermore, according to (2) and (3), the airgap specific permanence Λ_g can be derived as:

$$\Lambda_g(\theta_s,t)\approx\frac{g}{\mu_0}\frac{\Lambda_s(\theta_s)\Lambda_r(\theta_s,t)}{|\Lambda|} \tag{4}$$

where $|\Lambda|$ is the airgap length and unit specific permanence, respectively.

Base on the above analysis, the airgap flux density can be deduced to

$$\begin{aligned} &B_g(\theta_s,t)=F(\theta_s)\Lambda_g(\theta_s,t) \\ &=\frac{g}{\mu_0}\sum_{k=1}^{3,5,7,\cdots}F_k\sin\left(\frac{kN_s}{4}\theta_s\right)* \\ &\left[\frac{\Lambda_{s0}\Lambda_{r0}}{4}+\frac{\Lambda_{r0}}{2}\sum_{i=1}^{\infty}\Lambda_{si}\cos\left(\frac{iN_s}{2}\theta_s\right)+\right. \\ &\frac{\Lambda_{s0}}{2}\sum_{j=1}^{\infty}\Lambda_{rj}\cos\left(jN_r(\theta_s-\theta_0-\omega_r t)\right)+ \\ &\left.\frac{1}{2}\sum_{i=1}^{\infty}\sum_{j=1}^{\infty}\Lambda_{si}\Lambda_{rj}\cos\left(\left(jN_r\pm\frac{iN_s}{2}\right)\theta_s-jN_s\theta_0-jN_s\omega_r t\right)\right] \end{aligned} \tag{5}$$

TABLE II
HARMONICS IN AIRGAP FLUX DENSITY

Pole-pair number	Elec. speed	Direction
$kN_s/4$	0	Static
$kN_s/4\pm iN_s/2$	0	Static
$kN_s/4+jN_r$	$-jN_r\omega_r$	Backward
$kN_s/4-jN_r$	$jN_r\omega_r$	Uncertain
$kN_s/4+iN_s/2+jN_r$	$-jN_r\omega_r$	Backward
$kN_s/4-iN_s/2-jN_r$	$jN_r\omega_r$	Uncertain
$kN_s/4-iN_s/2+jN_r$	$-jN_r\omega_r$	Uncertain
$kN_s/4+iN_s/2-jN_r$	$jN_r\omega_r$	Uncertain

Furthermore, the components of airgap flux density can be distinguished, and the detailed information is listed in Table II. Combined with (5), it can be seen that different sets of weight factors including k, i, and j can generate fruitful airgap flux density harmonics. By analyzing Table II, it can be

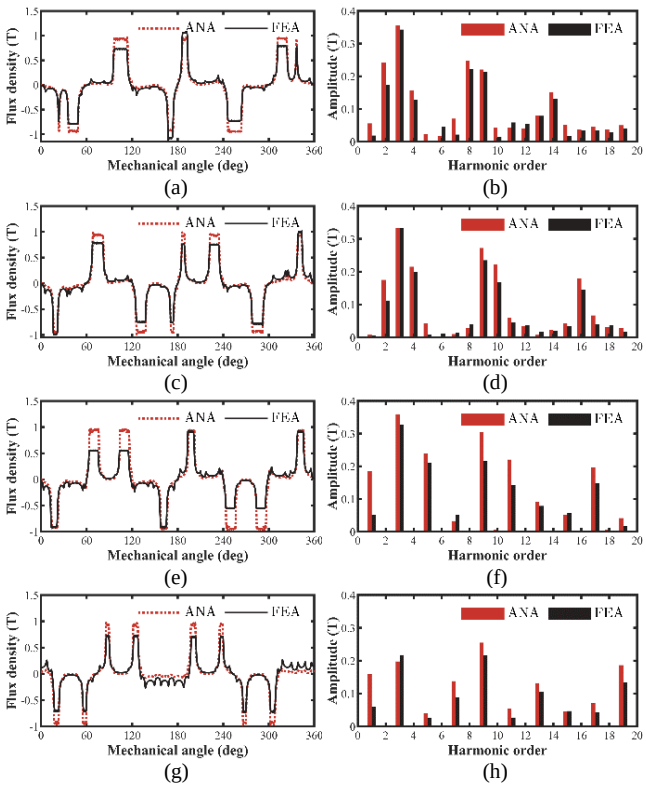

Fig. 3. Analysis of airgap flux density. (a) Flux density of 12s5p HEASPDSM. (b) Harmonic components of 12s5p HEASPDSM. (c) Flux density of 12s7p HEASPDSM. (d) Harmonic components of 12s7p HEASPDSM. (e) Flux density of 12s8p HEASPDSM. (f) Harmonic components of 12s8p HEASPDSM. (g) Flux density of 12s10p HEASPDSM. (h) Harmonic components of 12s10p HEASPDSM.

observed that these harmonics possess distinct pole-pair numbers, velocities, and movement directions. For several sets of harmonics with uncertain directions, such as those with pole-pair number of $kN_s/4–jN_r$, when $kN_s/4$ is greater than jN_r, this harmonic rotates in the forward direction; when $kN_s/4$ is smaller than jN_r, this harmonic reverses its rotation.

Fig. 3 shows the waveforms of flux density and harmonic components of four HEASPDSMs. It can be found that each airgap flux density component can be generated by multiple sets of modulation factors (k, i, j); for example, the 2nd harmonic of 12s7p HEASPDSM can be generated by (1, 1, 1), (2, 1, 2), etc. A comparative analysis of the harmonic spectra shows that changes in pole-pair combinations lead to remarkable differences in the amplitude and distribution of harmonics, while the dominant harmonic orders vary significantly. These differences originate from the structural dependence of magnetic field harmonics in HEASPDSMs, and they lay a fundamental basis for quantifying the contribution of individual harmonics to torque generation. Harmonics with higher amplitudes at specific orders can either enhance or deteriorate torque production, depending on their interaction with the machine's structural and magnetic properties.

B. Electromagnetic Torque Model with Spatial Harmonics

Firstly, the function expression of phase A winding of the HEASPDSM is presented by

$$N_{\mathrm{A}}(\theta_{\mathrm{s}})=\sum_{h=1}^{\infty}N_h\cos(\omega_{\mathrm{N}}h\theta_{\mathrm{s}}) \tag{6}$$

When N_{r} is odd, it will get

$$\begin{cases}\omega_{\mathrm{N}}=2\\ N_h=\dfrac{N_{\mathrm{c}}}{\pi h^2\left(\dfrac{\alpha+\beta_{\mathrm{s}}}{2}-\dfrac{2\pi}{N_{\mathrm{s}}}\right)}\left[\cos\left(\dfrac{4\pi h}{N_{\mathrm{s}}}\right)-\cos\left(h\left(\alpha+\beta_{\mathrm{s}}\right)\right)\right]\end{cases} \tag{7}$$

When N_{r} is even, it will get

$$\begin{cases}\omega_{\mathrm{N}}=1\\ N_h=\dfrac{N_{\mathrm{c}}}{\pi h^2\left(\dfrac{\alpha+\beta_{\mathrm{s}}}{2}-\dfrac{2\pi}{N_{\mathrm{s}}}\right)}*\\ \left[2\cos\left(\dfrac{2\pi h}{N_{\mathrm{s}}}\right)-2\cos\left(h\left(\dfrac{\alpha+\beta_{\mathrm{s}}}{2}\right)\right)-\right.\\ \cos\left(h\left(\pi-\dfrac{2\pi}{N_{\mathrm{s}}}\right)\right)+\cos\left(h\left(\pi-\dfrac{\alpha+\beta_{\mathrm{s}}}{2}\right)\right)-\\ \left.\cos\left(h\left(\pi+\dfrac{2\pi}{N_{\mathrm{s}}}\right)\right)+\cos\left(h\left(\pi+\dfrac{\alpha+\beta_{\mathrm{s}}}{2}\right)\right)\right]\end{cases} \tag{8}$$

where N_{A} is the Winding function of phase A; N_h is the Fourier coefficient; ω_{N} is the pole pair number; h is the Fourier order; N_{c} the turns of armature winding. Combined with (5), the flux linkage of phase A can be derived by

$$\begin{cases}\psi_{\mathrm{A}}(t)=\dfrac{R_{\mathrm{si}}+R_{\mathrm{ro}}}{2}L\int_0^{2\pi}B_{\mathrm{g}}(\theta_{\mathrm{s}},t)N_{\mathrm{A}}(\theta_{\mathrm{s}})\mathrm{d}\theta_{\mathrm{s}}\\ \chi(\theta_{\mathrm{s}},t)=B_{\mathrm{g}}(\theta_{\mathrm{s}},t)N_{\mathrm{A}}(\theta_{\mathrm{s}})=\sum_{n=1}^{\infty}\chi_n\end{cases} \tag{9}$$

where R_{si}, R_{ro}, and L are the inner radius of stator, the outer radius of rotor, and the length of motor, respectively; χ_n is the set of harmonics.

As the air-gap flux density and winding function both comprise a substantial number of harmonics, the solution for flux linkage is the integration of fundamental waves with a period of 2π and their multiple-frequency harmonics. Herein, only when $\partial\chi_n/\partial\theta_{\mathrm{s}}=0$, that is, when the pole pair number of χ_n with respect to θ_{s} is zero, will this harmonic component contribute to the generation of flux linkage.

Furthermore, the back-EMF of phase A can be derived as

$$E_{\mathrm{A}}=\mathrm{d}\psi_{\mathrm{A}}/\mathrm{d}t \tag{10}$$

and the instantaneous electromagnetic torque is

$$T_{\mathrm{e}}=\frac{E_{\mathrm{A}}I_{\mathrm{A}}+E_{\mathrm{B}}I_{\mathrm{B}}+E_{\mathrm{C}}I_{\mathrm{C}}}{\omega_{\mathrm{r}}} \tag{11}$$

where I_{ABC} and E_{ABC} are the phase current and voltage. In order to make the average torque T_{avg} greater than zero, the electrical speed $\omega_{\mathrm{e}}=N_{\mathrm{r}}\omega_{\mathrm{r}}$. Upon comprehensive consideration of the aforementioned research, a novel harmonic visualization torque model can be derived. When N_{r} is odd, the expressions of average torque and torque ripple are shown

$$\begin{cases} T_{\text{avg}} = \dfrac{3\pi\left(R_{\text{si}}+R_{\text{ro}}\right)LgN_{\text{r}}I_{\text{m}}}{16\mu_0}\displaystyle\sum_{x=0}^{\infty}\sum_{z=0}^{\infty}\sum_{y=0}^{0}F_{1+2x}\Lambda_{\text{sz}}\Lambda_{\text{r}(1+2y)}\left(N_{h1}+N_{h2}-N_{h3}-N_{h4}\right)\left(1+2y\right)\cos\left(\left(1+2y\right)N_{\text{r}}\theta_0\right) \\ T_{\text{rip}} = \dfrac{3\pi\left(R_{\text{si}}+R_{\text{ro}}\right)LgN_{\text{r}}I_{\text{m}}}{16\mu_0}\displaystyle\sum_{x=0}^{\infty}\sum_{z=0}^{\infty}\sum_{y=1}^{\infty}F_{1+2x}\Lambda_{\text{sz}}\Lambda_{\text{r}(1+2y)}\Big[\left(N_{h1}+N_{h2}-N_{h3}-N_{h4}\right)\left(1+2y\right)\cos\left(\left(1+2y\right)N_{\text{r}}\theta_0+\left(2y\right)N_{\text{r}}\omega_{\text{r}}t\right)+ \\ \left(N_{h5}-N_{h6}-N_{h7}\right)\left(1+2y\right)\cos\left(\left(1+2y\right)N_{\text{r}}\theta_0+\left(2+2y\right)N_{\text{r}}\omega_{\text{r}}t\right)\Big] \end{cases} \tag{12}$$

$$\begin{cases} T_{\text{avg}} = \dfrac{3\pi\left(R_{\text{si}}+R_{\text{ro}}\right)LgN_{\text{r}}I_{\text{m}}}{16\mu_0}\displaystyle\sum_{\text{x}=0}^{\infty}\sum_{y=1}^{1}\sum_{z=0}^{\infty}F_{1+2x}\Lambda_{\text{sz}}\Lambda_{\text{ry}}\left(N_{h5}-N_{h6}-N_{h7}\right)y\cos\left(yN_{\text{r}}\theta_0\right) \\ T_{\text{rip}} = \dfrac{3\pi\left(R_{\text{si}}+R_{\text{ro}}\right)LgN_{\text{r}}I_{\text{m}}}{16\mu_0}\displaystyle\sum_{x=0}^{\infty}\sum_{y=2}^{\infty}\sum_{z=0}^{\infty}F_{1+2x}\Lambda_{\text{sz}}\Lambda_{\text{ry}}\Big[\left(N_{h1}+N_{h2}-N_{h3}-N_{h4}\right)y\cos\left(yN_{\text{r}}\theta_0+\left(y+1\right)N_{\text{r}}\omega_{\text{r}}t\right)+ \\ \left(N_{h5}-N_{h6}-N_{h7}\right)y\cos\left(yN_{\text{r}}\theta_0+\left(y-1\right)N_{\text{r}}\omega_{\text{r}}t\right)\Big] \end{cases} \tag{13}$$

as (12), where h1-h7 can be expressed by (14); when N_{r} is even, the expressions of average torque and torque ripple are shown as (13), where h1-h7 can be expressed by (15). I_{m} is the amplitude of phase current; T_{rip} is the torque ripple.

In accordance with the derivation and analysis of the aforementioned torque expression previously presented, the model can directly obtain an effective combination of modulation coefficients. Subsequently, components like flux density can be screened, which is facilitating the comprehension of the operating principle of HEASPDSM. For example, in the case of a 12s8p HEASPDSM, based on (13) and (15), effective modulation coefficient combinations (k, i, j, h) can be directly obtained, such as (3, 1, 1, 7), (5, 1, 1, 1), (5, 2, 1, 19), and so forth.

$$\begin{cases} h1 = \left(N_{\text{s}}+4N_{\text{r}}\right)/8+N_{\text{s}}\left(x+z\right)/4+N_{\text{r}}y \\ h2 = \left(N_{\text{s}}+4N_{\text{r}}\right)/8+N_{\text{s}}\left(x-z\right)/4+N_{\text{r}}y \\ h3 = -\left(\left(N_{\text{s}}-4N_{\text{r}}\right)/8+N_{\text{s}}\left(x+z\right)/4-N_{\text{r}}y\right) \\ h4 = -\left(\left(N_{\text{s}}-4N_{\text{r}}\right)/8+N_{\text{s}}\left(x-z\right)/4-N_{\text{r}}y\right) \\ h5 = -\left(\left(N_{\text{s}}+4N_{\text{r}}\right)/8+N_{\text{s}}\left(x-z\right)/4+N_{\text{r}}y\right) \\ h6 = \left(N_{\text{s}}-4N_{\text{r}}\right)/8+N_{\text{s}}\left(x+z\right)/4-N_{\text{r}}y \\ h7 = \left(N_{\text{s}}-4N_{\text{r}}\right)/8+N_{\text{s}}\left(x-z\right)/4-N_{\text{r}}y \\ h1, h2, \ldots h7 = m,\ \ m = 1, 2, 3, \ldots \end{cases} \tag{14}$$

$$\begin{cases} h1 = N_{\text{s}}/4+N_{\text{s}}\left(x+z\right)/2+N_{\text{r}}y \\ h2 = N_{\text{s}}/4+N_{\text{s}}\left(x-z\right)/2+N_{\text{r}}y \\ h3 = -\left(N_{\text{s}}/4+N_{\text{s}}\left(x+z\right)/2-N_{\text{r}}y\right) \\ h4 = -\left(N_{\text{s}}/4+N_{\text{s}}\left(x-z\right)/2-N_{\text{r}}y\right) \\ h5 = -\left(N_{\text{s}}/4+N_{\text{s}}\left(x-z\right)/2+N_{\text{r}}y\right) \\ h6 = N_{\text{s}}/4+N_{\text{s}}\left(x+z\right)/2-N_{\text{r}}y \\ h7 = N_{\text{s}}/4+N_{\text{s}}\left(x-z\right)/2-N_{\text{r}}y \\ h1, h2, \ldots h7 = 1+2m,\ \ m = 0, 1, 2, 3, \ldots \end{cases} \tag{15}$$

Furthermore, based on the aforementioned torque model, the contributions of each working harmonic within the modulation components, such as the MMF and the specific permeance, to the torque generation process can be quantitatively analyzed. Firstly, in accordance with (12) and (13), it is found that only the fundamental component in the rotor-specific permeance can generate the average torque. And the quantitative analysis of the working harmonics of the MMF and the stator specific permeance is depicted in Fig. 4. Taking the 12s7p HEASPDSM as an example, as shown in Fig. 4(b), for the MMF, the average torques generated by its 1st and 3rd harmonics are 3.38 and 1.72 N·m respectively, while the torque generated by the 5th harmonic is negative; for the stator specific permeance, the torques generated by its 1st, 3rd, and 5th harmonics are 3.69, 0.57, and 0.91 N·m respectively, while the torque generated by the 2nd harmonic is negative.

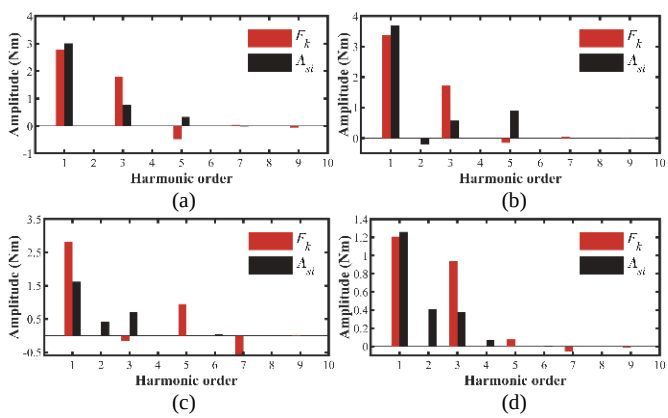

Fig. 4. The amplitude of the torque generated by the working harmonics. (a) 12s5p. (b) 12s7p. (c) 12s8p. (d) 12s10p.

IV. Simulation and Analysis

To validate the effectiveness of the proposed torque model, in this section, for the four HEASPDSMs in Section I, the torque model is employed to conduct an in-depth analysis of the impacts of key parameters on performance characteristics like average torque, torque ripple, and flux regulation capability. The results are compared with those from 2D finite element analysis.

A. Average Torque

To investigate the impact of different structural parameters on the average output torque of the aforementioned four HEASPDSMs, while maintaining other parameters constant and keeping excitation current zero, single-parameter scans are

performed. Firstly, as indicated by Fig. 5(a), it is demonstrated that the asymmetry angle exerts a considerably substantial influence on the average output torque. The rationale lies in that, while maintaining the slot fill factor of the two sets of windings, during the variation of this angle, it directly impacts the size of the overlapping area when the stator and rotor teeth form a magnetic circuit, thereby influencing the flux linkage and ultimately having an effect on the average torque. Eventually, the optimal angles for the four motors are 38°, 32°, 30°, and 22°, respectively (the number of rotor poles progresses from 5 to 10 in succession and remains consistent thereafter). In comparison with the FEA calculation results, the maximum errors of the analytical results obtained using the torque model are 5.7%, 6.0%, 6.8%, and 8.2% respectively.

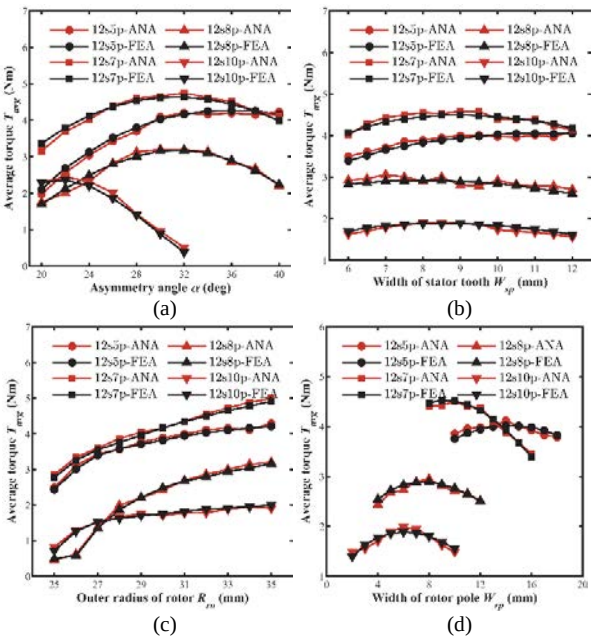

Fig. 5. The impact of different structural parameters on the average torque for different HEASPDSMs. (a) Asymmetry angle. (b) Width of stator tooth. (c) Outer radius of rotor. (d) Width of rotor pole.

Regarding the influence of stator and rotor tooth widths on the average torque, as depicted in Figs. 5(b) and 5(d), when the tooth width or pole width value is overly small, the magnetic reluctance of the main magnetic circuit is reduced, leading to easy saturation of the motor, which in turn reduces the magnetic load and consequently diminishes the torque. When the stator tooth width is excessively large, the number of turns of the motor winding is correspondingly decreased, resulting in a reduction of the electrical load of the motor and a weakening of its torque output capability. When the rotor pole width is unduly large, it is prone to overlap with the adjacent stator teeth, thereby causing a short circuit in the magnetic circuit, increasing the leakage flux of the main magnetic circuit and further reducing the torque. Thus, both sets of curves display a distribution that initially increases and then decreases. Analyzing the calculation results, for the stator tooth width, the optimal values are 11, 9, 8.5, and 8 mm, respectively, and the maximum analytical errors are 2.9%, 2.3%, 5.1%, and 5.6%, respectively. For the rotor pole width, the optimal values are 14.5, 9.5, 8, and 6 mm, respectively, and the maximum analytical errors are 3.1%, 2.5%, 3.9%, and 7.0% respectively.

Finally, in considering the impact of the rotor outer radius on the output torque and with reference to Fig. 5(c), in accordance with the principle of motor main dimension design, when the magnetic load and electrical load remain unchanged, a larger rotor outer diameter results in a greater motor output torque. The final results show that the maximum errors of the analytical method are 3.1%, 2.9%, 8.6%, and 11.2%.

B. Torque Ripple

The influences of main structural parameters on the torque ripple of the aforementioned four HEASPDSMs are shown in Fig. 6. From Fig. 6(a), it can be observed that when the asymmetry angles are 30°, 30°, 26°, and 30°, respectively, the torque ripple reaches its minimum value. The maximum analytical errors of the analytical results of the torque model in comparison with finite element analysis are 18.0%, 25.6%, 11.6%, and 8.8%, respectively. Regarding the influence of stator tooth width on torque ripple, as illustrated in Fig. 6(b), it reaches the optimum at 12, 9.5, 11, and 9 mm, respectively. Furthermore, the maximum analytical errors are 12.6%, 25.2%, 11.5%, and 9.1%, respectively. According to Fig. 6(c), when the rotor outer radii are 26, 32, 31, and 32 mm, respectively, the torque ripple of the four motors is minimized. Additionally, the maximum calculation errors of the two methods are 27.5%, 23.7%, 16.7%, and 8.1%, respectively. Finally, analyzing Fig. 6(d), the rotor pole width also has a substantial impact on the torque ripple. When the optimal values are 18, 14.5, 10.5, and 5 mm, respectively, the maximum analytical errors are 18.7%, 28.9%, 10.5%, and 8.8%, respectively.

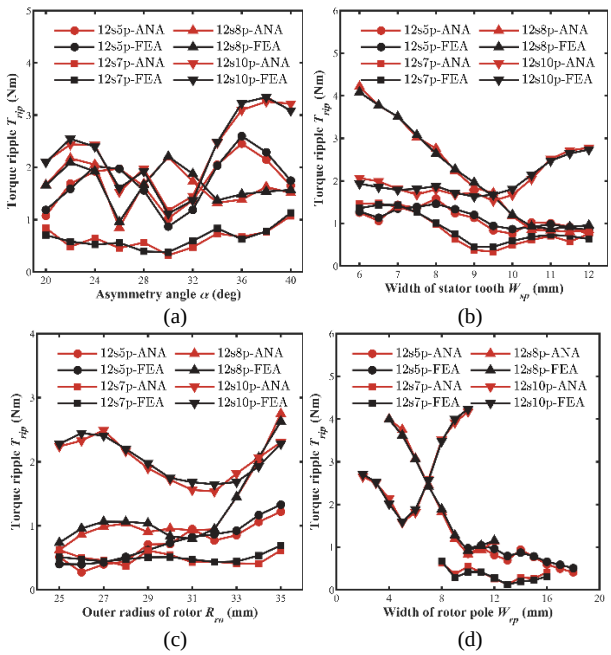

Fig. 6. The impact of different structural parameters on the torque ripple with different HEASPDSMs. (a) Asymmetry angle. (b) Width of stator tooth. (c) Outer radius of rotor. (d) Width of rotor pole.

C. Flux Regulation Ability

The flux regulation coefficient is defined as

$$K_{\psi}=\frac{\psi_{\text{enhanced}}}{\psi_{\text{weakened}}} \tag{16}$$

where ψ_{enhanced} and ψ_{weakened} are the enhanced flux linkage and weakened flux linkage, and the greater the K_{ψ}, the better the flux regulation ability. Refer to [20], when the HEASPDSM operates in the constant torque region with "$i_{\text{d}}=0$" control strategy, the following relationship exists

$$\begin{cases} T_{\max}=1.5N_{\text{r}}i_{\text{q}}\psi_{\text{enhanced}}=1.5N_{\text{r}}i_{\text{q}}\left(\psi_{\text{pm}}+M_{\text{ce}}I_{\text{e}}\right) \\ T_{\min}=1.5N_{\text{r}}i_{\text{q}}\psi_{\text{weakened}}=1.5N_{\text{r}}i_{\text{q}}\left(\psi_{\text{pm}}-M_{\text{ce}}I_{\text{e}}\right) \end{cases} \tag{17}$$

where $T_{\max}$ and $T_{\min}$ are the maximum and minimum value of output torque; i_{q}, ψ_{pm}, M_{ce} are the q-axis current, PM flux linkage and the mutual inductance of the two sets of windings. Due to the entire analysis in this manuscript is conducted under the premise that magnetic saturation of the motor is neglected, and combined with (17), the flux regulation coefficient can be restructured as

$$K_{\psi}=\frac{\psi_{\text{enhanced}}}{\psi_{\text{weakened}}}=\frac{T_{\max}}{T_{\min}} \tag{18}$$

Therefore, while keeping other parameters unchanged, the influence trends of the main structural parameters on the four HEASPDSMs are presented as shown in Fig. 7.

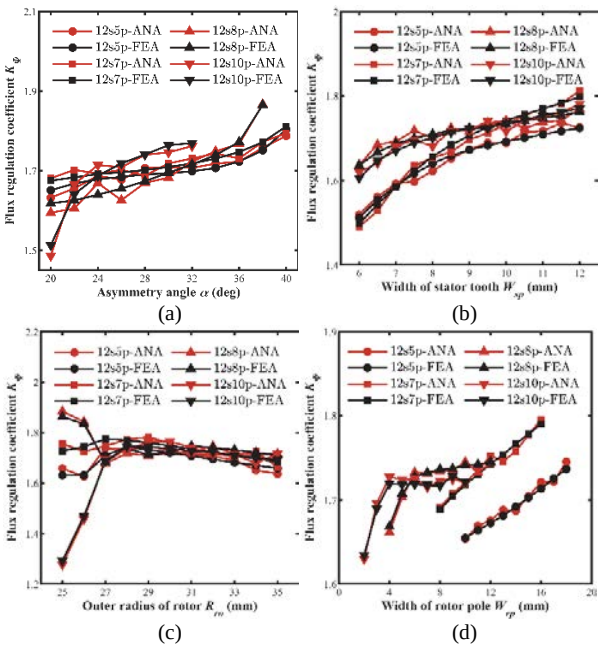

Fig. 7. The impact of different structural parameters on the flux regulation capability with different HEASPDSMs. (a) Asymmetry angle. (b) Width of stator tooth. (c) Outer radius of rotor. (d) Width of rotor pole.

Firstly, an analysis is conducted on the impact of the stator asymmetry angle on the flux regulation capacity. As illustrated in Fig. 7(a), it can be noted that as the stator asymmetry angle increases, the flux regulation capability of the motor generally presents an ascending tendency. The reason for this phenomenon is that when keeping the slot fill factor unchanged, as the angle grows, the turns of the excitation winding increase, leading to an elevation in the MMF of the excitation winding. Consequently, both the magnetizing and demagnetizing effects on the magnetic circuit are enhanced, thereby boosting the flux regulation capacity of the motor. In comparison with the FEA method, the maximum calculation errors of the analytical method proposed in this paper are respectively 3.1%, 2.0%, 3.7%, and 4.5%.

Secondly, upon observing Figs. 7(b) and 7(d), it can be seen that the flux regulation capacity of the motor increases with the increase in stator tooth width and rotor pole width. The main cause for this trend is that as these two parameters increase, the reluctance of the main magnetic circuit diminishes. However, based on the calculation results, it is discovered that the increase in stator tooth width has a weaker impact on the flux regulation capacity compared to the rotor pole width. The main reason for this is that as the stator tooth width increases, while the reluctance of the magnetic circuit decreases, the turns of the excitation winding will also decrease due to the reduction in slot area, thereby reducing the excitation MMF. Regarding the maximum analytical errors of the two methods, in the analysis process of stator tooth width, they are 3.5%, 3.8%, 2.2%, and 4.1% respectively, and for rotor pole width are 1.5%, 3.9%, 2.5%, and 5.5% respectively.

Finally, with respect to the impact of the rotor outer radius on the flux regulation capacity, the optimal values are 28, 29, 25, and 29 mm, and the maximum analytical errors are 3.7%, 1.9%, 3.3%, and 6.1%.

Moreover, based on the foregoing analysis, the following is a comparative analysis of electromagnetic torque with different excitation conditions for four HEASPDSMs.

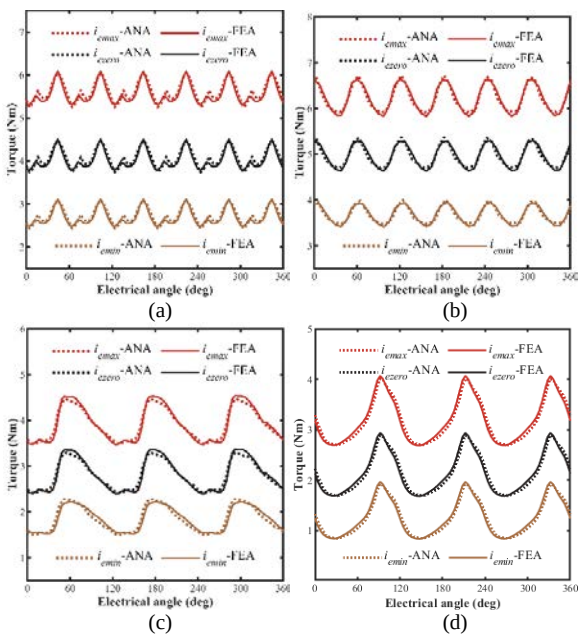

Fig. 8. The electromagnetic torque with different excitation conditions for HEASPDSMs. (a) 12s5p. (b) 12s7p. (c) 12s8p. (d) 12s10p.

As illustrated in Fig. 8, the output torque waveforms of the four HEASPDSMs under three typical conditions including maximum magnetizing condition, permanent magnet condition, and maximum demagnetizing condition are displayed. The four sets of waveforms clearly demonstrate the regulatory effect of the excitation current on the magnetic

field and output torque. Additionally, the results of the analytical calculation using the proposed torque model are largely in line with FEA.

V. Experiment and Analysis

To further validate the effectiveness of the torque model presented in this paper, a 12s7p HEASPDSM is designed and manufactured. Fig. 9 presents the pictures of its stator, rotor, and laminations. Fig. 10 shows the platform of HEASPDSM, which is coupled to a hysteresis brake via a torquemeter, where the hysteresis brake is working as a load during the experiment. Main parameters of the HEASPDSM are listed in Table III.

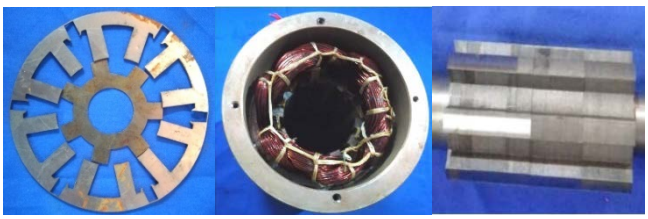

(a) (b) (c)

Fig. 9. The prototype of 12s7p HEASPDSM. (a) Iron laminations. (b) Stator. (c) Rotor.

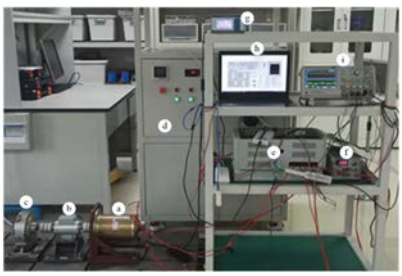

Fig. 10. Platform of HEASPDSM.

TABLE III
MAIN PARAMETERS OF 12S7P HEASPDSM

Term	Value
Outer diameter of stator/mm	120
Stack length/mm	100
Asymmetry angle/mm	27.4
Outer diameter of rotor/mm	64
Width of stator tooth/mm	9.4
Width of rotor pole/mm	10.3
Length of airgap/mm	0.5
Rated power/W	320
Rated speed/(r/min)	600
Armature current (RMS)/A	3
Excitation current/A	4
Turns of armature winding	85
Turns of excitation winding	100

Firstly, the no-load line-to-line back-EMF test is conducted on the platform, and the analytical calculation is performed using (14) simultaneously, and a comparative analysis is carried out in conjunction with the FEA results. Referring to Fig. 11, it can be observed that under the three excitation conditions, the amplitudes of the line-to-line back-EMF measured experimentally are 64.9, 82.4, and 103.6 V respectively. The values obtained by the analytical method are 69.5, 91.9, and 112.5 V, and those obtained by the FEA method are 68.5, 89.9, and 114.5 V. Furthermore, under the three conditions, compared with the experimental results, the errors of the analytical method are 7.1%, 11.5%, and 8.6% respectively. And in comparison, with the FEA results, they are 1.5%, 2.2%, and 1.8%, respectively. It shows that the results obtained by the three methods are obviously consistent with each other.

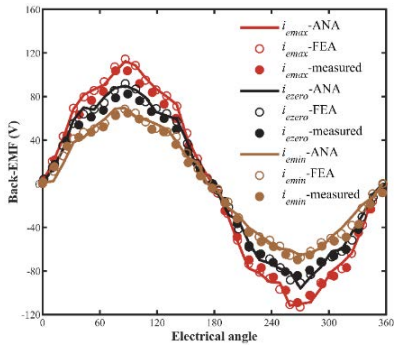

Fig. 11. No-load line-to-line back-EMF of 12s7p HEASPDSM.

Furthermore, the average torque of the 12s7p HEASPDSM prototype is analyzed and compared by utilizing the aforementioned three methods. The results are presented in Fig. 12. It can be observed that as the amplitude of the armature current increases, the average torque correspondingly rises. Under the three excitation conditions, the maximum errors of the analytical method compared to the experimental results are 13.4%, 10.6%, and 18.0% respectively. In contrast to the finite element method, the maximum errors are 8.1%, 5.5%, and 7.6% respectively. The relatively large error in the experimental results is due to the fact that the effects of frictional losses as well as stray losses are not considered in the process of analyzing and simulating results.

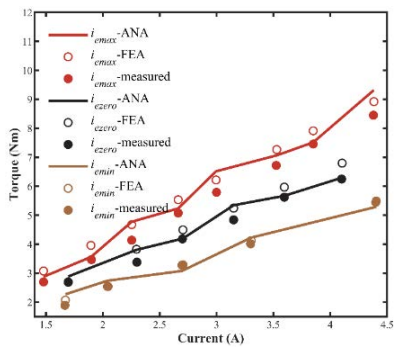

Fig. 12. Average torque of 12s7p HEASPDSM.

VI. Conclusions

This paper proposes a novel torque evaluation model for HEASPDSMs to tackle the limitation of traditional MFMA in torque analysis, which only identifies airgap flux harmonics but fails to quantify the structure-harmonic-torque correlation. It fills the research gap of quantitative analysis for the "structure-modulation component-harmonic-torque" link. The model's core innovations are realizing simultaneous quantitative evaluation of average torque and torque ripple by

directly using stator/rotor modulation components, and quantifying individual harmonic torque contributions while associating them with structural parameters. Validation via FEA single-parameter scans on four HEASPDSMs with varied pole-pair combinations and experiments on a 12s7p prototype confirms its accuracy. Overall, this work lays a quantitative foundation for HEASPDSM optimization and advances the adoption of high-performance electric machines in next-generation IMDs.

REFERENCES

[1] S. P. Wu, C. C. Tian, and W. D. Zhao *et al*., "Design and Analysis of an Integrated Modular Motor Drive for More Electric Aircraft," *IEEE Trans. on Transport. Electrific.*, vol. 6, no. 4, pp. 1412-1420, Dec. 2020.

[2] A. Ebrahimian, S. Iman Hosseini Sabzevari, and W. A. Khan *et al*., "Design and Experimental Validation of a High-power-density GaN-based Inverter Module for Integrated Modular Motor Drives in All-electric Aircraft Applications," *IEEE J. of Emerg. and Sel. Topics in Power Electron.*, vol. 13, no. 4, pp. 4504-4520, Aug. 2025.

[3] M. Bahrami-Fard, T. Y. Chen, and E. A. Winchell *et al*., "Integrated Induction Motor Drive for Variable Speed Industrial Applications," *IEEE Trans. on Power Electron.*, vol. 40, no. 5, pp. 7176-7188, May 2025.

[4] X. Zhang, W. Zhang, and X. Y. Liang *et al*., "Performance Analysis and Comparison for Two Topologies of Flux-switching Permanent Magnet Machine," *CES Trans. on Elect. Mach. and Syst.*, vol. 4, no. 3, pp. 190-197, Sept. 2020.

[5] Z. Q. Zhu, W. Q. Chu, and Y. Guan, "Quantitative Comparison of Electromagnetic Performance of Electrical Machines for HEVs/EVs," *CES Trans. on Elect. Mach. and Syst.*, vol. 1, no. 1, pp. 37-47, Mar. 2017.

[6] W. Xu, Y. S. Zhang, and G. H. Du *et al*., "No-load Performance Analysis of an Asymmetric-pole Single-phase Doubly Salient Permanent Magnet Machine," *IEEE Trans. on Ind. Electron.*, vol. 68, no. 4, pp. 2907-2918, Apr. 2021.

[7] X. Y. Zhu, and M. Cheng, "A Novel Stator Hybrid Excited Doubly Salient Permanent Magnet Brushless Machine for Electric Vehicles," in *Proc. of 2005 Int. Conf. on Elect. Mach. and Syst.*, Nanjing, China, Sept. 2005, pp. 412-415.

[8] K. T. Chau, J. Z. Jiang, and Y. Wang, "A Novel Stator Doubly Fed Doubly Salient Permanent Magnet Brushless Machine," *IEEE Trans. on Magn.*, vol. 39, no. 5, pp. 3001-3003, Sept. 2003.

[9] Z. R. Zhang, Y. Y. Tao, and Y. G. Yan, "Investigation of a New Topology of Hybrid Excitation Doubly Salient Brushless DC Generator," *IEEE Trans. on Ind. Electron.*, vol. 59, no. 6, pp. 2550-2556, Jun. 2012.

[10] J. F. Jiang, S. X. Niu, and X. Zhao, "Quantitative Analysis of Hybrid-excited Doubly Salient Machine with Subslot Bottom PMs and Its Comparative Study," *IEEE Trans. on Ind. Electron.*, vol. 70, no. 5, pp. 4558-4569, May 2023.

[11] M. J. He, W. Xu, and J. G. Zhu *et al*., "A Novel Hybrid Excited Doubly Salient Machine with Asymmetric Stator Poles," *IEEE Trans. on Ind. Appl.*, vol. 55, no. 5, pp. 4723-4732, Sept.-Oct. 2019.

[12] M. Cheng, P. Han, and W. Hua, "General Airgap Field Modulation Theory for Electrical Machines," *IEEE Trans. on Ind. Electron.*, vol. 64, no. 8, pp. 6063-6074, Aug. 2017.

[13] P. X. Wang, W. Hua, and G. Zhang *et al*., "Principle of Flux-switching Permanent Magnet Machine by Magnetic Field Modulation Theory Part I: Back-electromotive-force Generation," *IEEE Trans. on Ind. Electron.*, vol. 69, no. 3, pp. 2370-2379, Mar. 2022.

[14] P. X. Wang, W. Hua, and G. Zhang *et al*., "Principle of Flux-switching PM Machine by Magnetic Field Modulation Theory Part II: Electromagnetic Torque Generation," *IEEE Trans. on Ind. Electron.*, vol. 69, no. 3, pp. 2437-2446, Mar. 2022.

[15] X. Y. Ma, G. J. Li, and G. W. Jewell *et al*., "Quantitative Analysis of Contribution of Air-gap Field Harmonics to Torque Production in Three-phase 12-slot/8-pole Doubly Salient Synchronous Reluctance Machines," *IEEE Trans. on Magn.*, vol. 54, no. 9, pp. 1-11, Sept. 2018.

[16] Y. Li, H. Yang, and H. Y. Lin, "Comparative Study of Torque Production Mechanisms in Stator and Rotor Consequent-pole Permanent Magnet Machines," *IEEE Trans. on Transport. Electrific.*, vol. 7, no. 4, pp. 2694-2704, Dec. 2021.

[17] D. W. Li, R. H. Qu, and J. Li *et al*., "Analysis of Torque Capability and Quality in Vernier Permanent-magnet Machines," *IEEE Trans. on Ind. Appl.*, vol. 52, no. 1, pp. 125-135, Jan.-Feb. 2016.

[18] L. Fang, D. W. Li, and X. Ren *et al*., "A Novel Permanent Magnet Vernier Machine with Coding-shaped Tooth," *IEEE Trans. on Ind. Electron.*, vol. 69, no. 6, pp. 6058-6068, Jun. 2022.

[19] L. Fang, D. W. Li, and X. Ren *et al*., "A Quantitative Air-gap Construction Method to Maximize Torque of Vernier PM Machines," *IEEE Trans. on Transport. Electrific.*, vol. 9, no. 1, pp. 463-473, Mar. 2023.

[20] W. Xu, C. Cao, and Y. S. Zhang *et al*., "Improved Flux-weakening Method with Excitation Current Distribution for Hybridly Excited Asymmetric Stator Pole Doubly Salient Machine based on Electrical Vehicle," *IEEE J. of Emerg. and Sel. Topics in Power Electron.*, vol. 11, no. 2, pp. 1385-1396, Apr. 2023.

Chen Cao received the B.E. degree in electrical engineering in 2020 from the University of Electronic Science and Technology of China, Chengdu, China, and the M.E. degree in electrical engineering in 2022 from Huazhong University of Electronic Science and Technology, Wuhan, China. He is currently working toward a Ph.D. degree in electrical engineering from Huazhong University of Electronic Science and Technology.

His research interests include the design, modeling and control of high-power/torque-density electric machines.

Wei Xu (Fellow, IEEE) received the B.E. and M.E. degrees from Tianjin University, Tianjin, China, in 2002 and 2005, respectively, and the Ph.D. degree from the Institute of Electrical Engineering, Chinese Academy of Sciences (IEECAS), Beijing, China, in 2008, all in electrical engineering.

He is currently a professor with Institute of Electrical Engineering, Chinese Academy of Sciences, Beijing, China. His research interests include design and control for linear machines and drives.

Jian Ge received the B.E., M.E., and Ph.D. degrees in electrical engineering from Huazhong University of Science and Technology, Wuhan, China, in 2016, 2019, and 2022, respectively.

He is currently an assistant research fellow with the State Key Laboratory of High-Density Electrical Energy Conversion, Huazhong University of Science and Technology. His research interests include linear induction machines, high-power/torque-density electric machines and brushless doubly-fed machines.

Bin Du received the M.E. degree in materials processing engineering from Huazhong University of Science and Technology, Wuhan, China, in 2009.

He is currently the vice minister of the Science and Technology Development Department and senior engineer at China National Electric Apparatus Research Institute Co., Ltd. His research interest is intelligent manufacturing.

Zhongyong Chen received the B.E. degree in physics from Shaanxi Normal University, Xi'an, China, in 2001, and the Ph.D. degree from the Institute of Plasma Physics, Chinese Academy of Sciences, Beijing, China, in June 2006.

He is currently a professor with the Huazhong University of Science and Technology, Wuhan, China, and he is an expert of the International Tokamak Physics Activity (ITPA) Topical Group on Magnetohydrodynamics (MHD), Disruptions and Control Committee.

Chuanjia Zhang received the B.E. degrees in electrical engineering from Shandong University, Shandong, China, in 2006.

He is currently the vice president of Electromechanical Apparatus and Equipment Division of CVC Testing Technology Co., Ltd., focusing on quality and technical service research in the fields of safety, performance, and reliability of mechanical, robot, electric motor, capacitor, and other products.

Lili Kang received the B.E. and M.S degrees in measurement and control technology and instrumentation from Yanshan University, Hebei Province, China, in 2006 and 2009, and the Ph.D. degree in electrical engineering, from the School of Electrical and Information Engineering, Tianjin University, Tianjin, China, in 2022.

She is currently an associate professor with Intelligent Manufacturing College, Tianjin Sino-German University of Applied Sciences, Tianjin, China. Her research interests include the design and control of motors.

Lei Zhang received the B.E. degree in mechanical manufacturing technology and equipment from Hebei Polytechnic University, Hebei, China, in 1997.

He is currently the Deputy Chief Engineer of Technology at CRRC Tangshan Co., Ltd., focusing on maglev transportation products development and digital design technology.